CERN-SPSC-2005-022
SPSC-M-736
23.06.2005

Status Report of the CAST Experiment

The CAST Collaboration

CEA-Saclay – CERN – Hellenic Open University Patras – Lawrence Livermore National Laboratory – Max-Planck-Institut für extraterrestrische Physik – Max-Planck-Institut für Physik – National Center for Scientific Research Demokritos – Rudjer Boskovic Institute – Russian Academy of Science – TU Darmstadt – University of British Columbia – University of Chicago – Universität Frankfurt – Universität Freiburg – University of Patras – University of South Carolina – University of Thessaloniki – Universidad de Zaragoza

1 Solar Axion Model

For the interpretation and analysis of the CAST data the solar axion flux and its spatial and spectral distribution have to be known. Previous estimates of the solar axion flux are based on the standard solar model (SSM) of 1982 (van Bibber et al., 1989). Since the solar model has changed substantially since then, we recalculated the axion flux parameters based on the most recent solar model BP2004 (Bahcall & Pinsonneault, 2004). In the left part of Fig. 1 we compare the differential axion flux of the 1982 and 2004 solar models. Even though a large number of details has changed, standard solar models and their neutrino predictions have remained remarkably robust. The same is true for the axion flux prediction that depends only mildly on the exact solar model. Note that the treatment of the Primakoff effect (screening effects) is somewhat approximate so that the total flux is never more precise than within a few percent anyway.

In addition, we have calculated the solar surface luminosity $\varphi_a(E, r)$. In the right part of Fig. 1 a contour plot of this quantity is given as a function of axion energy E and dimensionless radial coordinate r on the solar disk. As an analytical representation of the differential axion spectrum we get:

$$\frac{d\Phi_{\mathrm{a}}}{dE} = g_{10}^2 \, \frac{E^{2.481}}{e^{E/1.205}} \, 6.020 \times 10^{10} \, \mathrm{cm}^{-2} \, \mathrm{s}^{-1} \, \mathrm{keV}^{-1} \tag{1}$$

compared to the result of van Bibber et al. (1989) which is:

$$\frac{d\Phi_{\mathrm{a}}}{dE} = g_{10}^2 \frac{E_{\mathrm{keV}}^3}{e^{E_{\mathrm{keV}}/1.08} - 1} \, 4.02 \times 10^{10} \mathrm{cm}^{-2} \, \mathrm{s}^{-1} \, \mathrm{keV}^{-1} \tag{2}$$

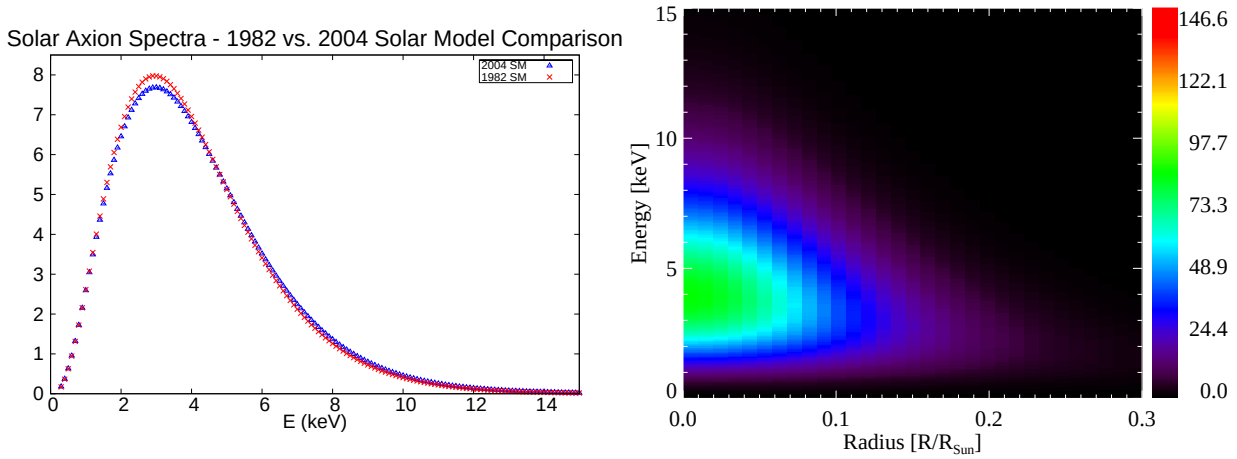

Figure 1: Left: Comparison between the solar axion spectrum calculated from the standard solar model of 1982 and the modern standard solar model BP2004. Right: Axion surface luminosity of the solar disk as a function of energy and the radius of the sun normalized to the solar radius R_{Sun}.

where $E_{\text{keV}} = E/\text{keV}$ is the axion energy and

$$g_{10} = \frac{g_{\text{a}\gamma}}{10^{-10}\,\text{GeV}^{-1}}\,. \tag{3}$$

Furthermore, recent theoretical results of members of our collaboration yield a new cosmological mass limit for axions $m_a < 1.05\,\text{eV}$ ($95\%\,\text{CL}$, Hannestad et al., 2005). This limit nicely coincides with the highest axion mass CAST is sensitive to during Phase II and gives the opportunity to close the remaining gap between cosmological and experimental limits on the axion to photon coupling $g_{\text{a}\gamma}$.

2 Scientific Results

At the end of 2004 we finished the analysis of the data acquired in 2003. A summary of the data sets measured with the different detectors of CAST and the respective exposure times is given in Table 1. The analysis reveals no significant excess signal over background and allows us to set a new upper limit on the axion to photon coupling $g_{\text{a}\gamma}$. For each data set an individual upper limit on $g_{\text{a}\gamma}$ could be derived, which finally were statistically combined to the result published by our collaboration (Zioutas et al., 2005, for the CAST collaboration):

$$g_{\text{a}\gamma} \lesssim 1.16 \times 10^{-10}\,\text{GeV}^{-1}\,(95\%\,\text{CL}) \tag{4}$$

This upper limit, due to coherence effects valid for $m_{\text{a}} < 0.02\,\text{eV}$, is a factor of 5 more stringent compared to previous laboratory constraints and is already competitive with limits derived from astrophysical considerations. Fig. 2 shows the corresponding combined upper limit in comparison to previous results. The analysis of the 2004 data is still in progress and will further improve the upper limit, especially when exploiting the full potential of the X-ray telescope.

3 Cryogenics and Magnet Operation

During the CAST Phase I in 2004 run we had recurrent problems with a He leak in the cryostat, causing magnet temperature instabilities which would cause complications during Phase II magnet

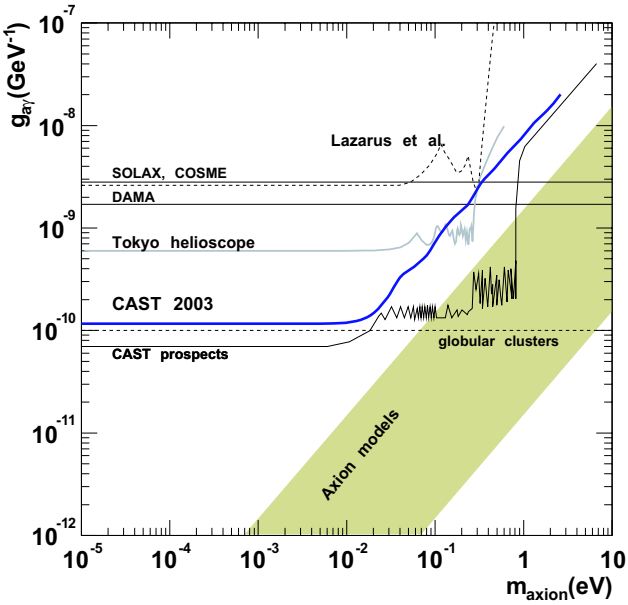

Figure 2: Upper limit (95% CL) of the axion to photon coupling constant $g_{a\gamma}$ depending on the axion mass m_{axion} derived from the data of 2003 (Zioutas et al., 2005). The result of earlier experiments like, e.g. *SOLAX*, *COSME*, *DAMA*, and the Tokyo helioscope. An interpretation of the singal observed by PVLAS in terms of axion production leads to a coupling constant of $2.5 \times 10^{-5}\,\text{GeV}^{-1}$, which does not seem to be in agreement with the limits shown.

operation. After the Phase I run was completed, the planned opening of the cryostat allowed us to carry out a long series of systematic tests to localize the super fluid helium leak. Unfortunately, with the magnet at room temperature and using a leak detector in sniffing mode, it was not possible to localize the leak, other than to say that it is very likely to be from the liquid helium tank in the top of the MFB. As had been foreseen for Phase II operation, we have installed two new turbo pumps on the main isolation vacuum, increasing our pumping capacity from $400\,\text{L/s}$ to $1500\,\text{L/s}$.

Since the installation of the new pumps we monitored variations in the helium leak rate. Compared to the situation before, the leak rate is much more stable at a level of $1\text{–}2 \times 10^{-6}\,\text{mbar l/s}$. In addition the leak rate is independent of the magnet current between $0\text{–}12000\,\text{A}$. We are therefore currently seeing very little temperature instability in the beam pipes. The temperature changes from $1.78\text{–}1.79\,\text{K}$ when the magnet is powered at $12000\,\text{A}$ and $1.76\text{–}1.77\,\text{K}$ when the magnet current is off. During the planned quench tests the helium level obviously rises but the new pumps work well and expel the cryo-pumped helium liberated during the quench. We look forward to see

Table 1: Data sets of the 2003 data taking period included in our published result (Zioutas et al., 2005).

Data set	Tracking (h)	Background (h)	$(g^4_{a\gamma})_{\text{bestfit}}$ ($\pm 1\sigma$ error) (10^{-40} GeV^{-4})	χ^2_{null}/d.o.f	χ^2_{min}/d.o.f	$g_{a\gamma}$(95%) (10^{-10} GeV^{-1})
TPC	62.7	719.9	-1.1 ± 3.3	18.2/18	18.1/17	1.55
MM set A	43.8	431.4	-1.4 ± 4.5	12.5/14	12.4/13	1.67
MM set B	11.5	121.0	2.5 ± 8.8	6.2/14	6.1/13	2.09
MM set C	21.8	251.0	-9.4 ± 6.5	12.8/14	10.7/13	1.67
CCD	121.3	1233.5	0.4 ± 1.0	28.6/20	28.5/19	1.23

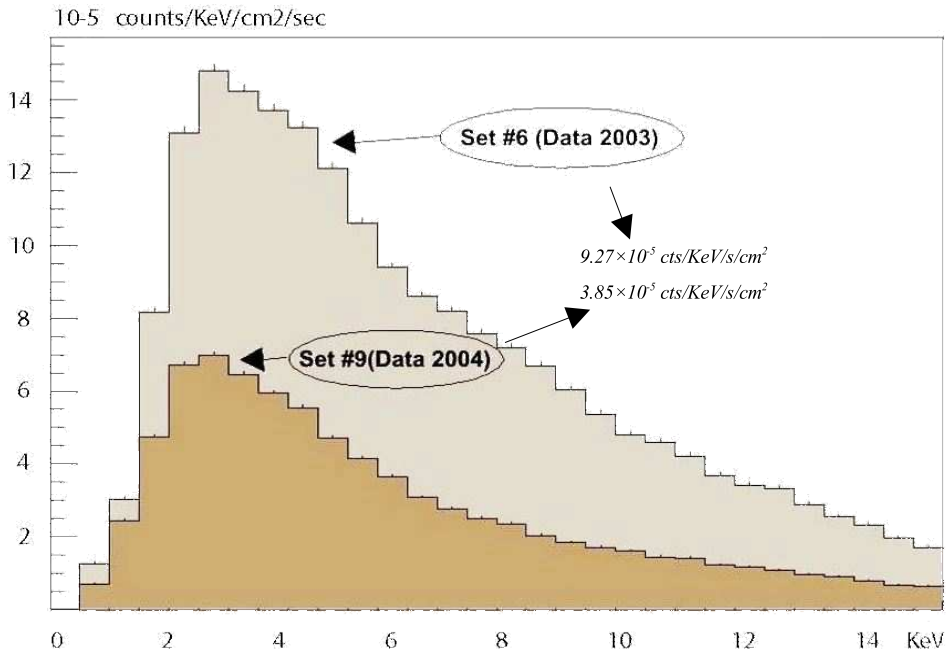

Figure 3: Comparison of the background level of the TPC detector between 2003 (copper box and nitrogen flux to suppress contamination by Radon) and 2004 (full shield).

the performance of the system during the planned quenches in the next few weeks.

4 The TPC Detector

The Time Projection Chamber (TPC) of the CAST experiment was operated continuously during the whole 2004 CAST data taking period. The main difference between 2003 and 2004 experimental setup were the operation of a new differential pumping system and improved passive and active shields for the detector.

Differential Pumping System The purpose of the differential pumping system is to decrease the effect of gas leaks towards the magnet and to minimize the possibility to damage the TPC windows due to sudden pressure changes or break down. The leak rate towards the magnet has been reduced more than one order of magnitude. As a result of the smooth operation of the TPC the total amount of data taken during 2004 is five times higher compared to 2003, which in turn leads to a better sensitivity for the final upper limit on $g_{a\gamma}$ in 2004.

Active and Passive Shield The installation of the passive shield has been finished in 2004. The final configuration for the TPC detector is composed of several layers of different material in order to reduce the experimental background. From the outside to the inside, the shield consists of a layer of 225 mm of polyethylene, 1 mm of cadmium, 25 mm of lead, and 5 mm thick copper box covering the TPC detector. The copper box is permanently flushed with nitrogen, creating an over pressure which decreases the Radon contamination close to the detector. An active shield was installed on top of the TPC in order to reject muon induced background in the TPC. The installation of the

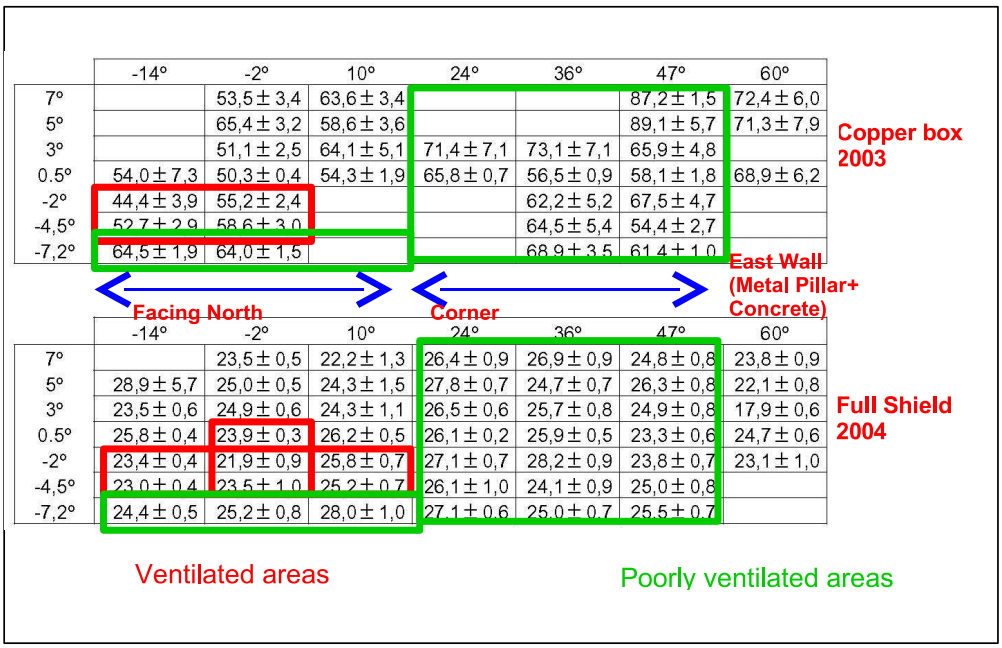

Figure 4: 2003/2004 background measurements in the energy range 3–7 keV given in units of counts/hour observed in the TPC.

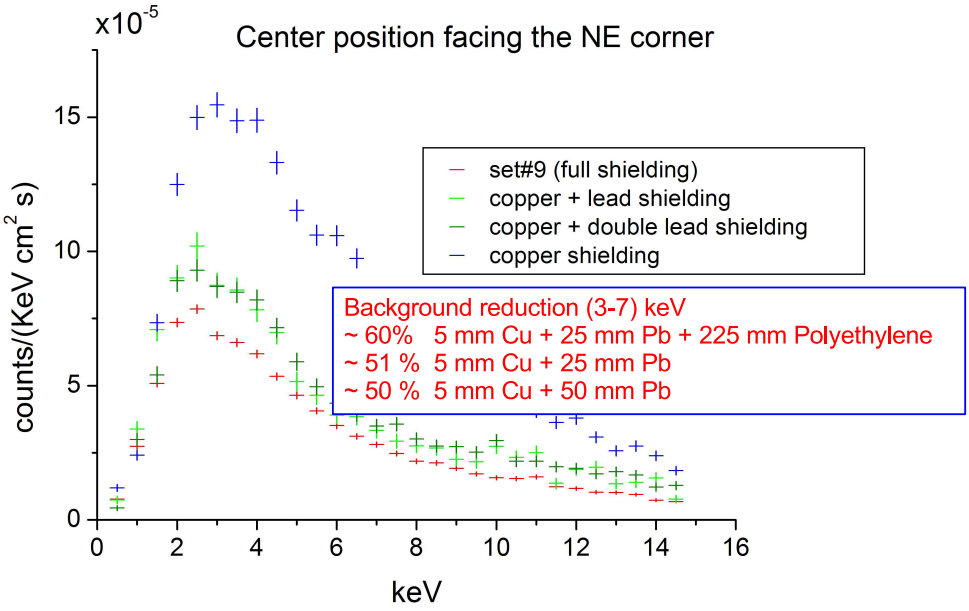

Figure 5: Improvement of the TPC background for different shielding compositions.

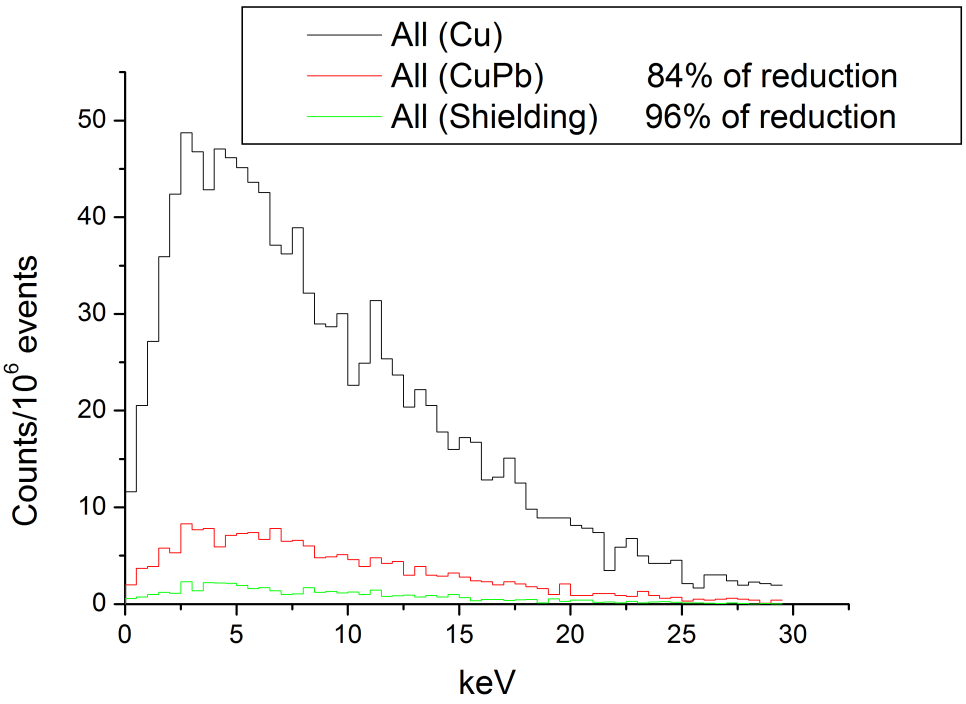

Figure 6: Simulated background for the TPC for ^{40}K.

shield has reduced the TPC background level over the whole energy range of the detector by a factor of 2.4 compared to the background level of 2003 (see Fig. 3). One of the most important advantages of the improved background suppression is the fact that the observed background is independant of the magnet pointing direction, which was not the case during the 2003 data taking period (see Fig. 4).

A complete set of simulations have been performed to get a better understanding of the environmental background. The results of the simulations confirm the experimental data and justify the shielding concept. The CAST site has a radioactive background dominated by radon, gamma sources (mainly the U and Th chains and Potassium) and cosmic neutrons. As a conclusion, we could say that the shielding reduces the background by a factor of about $\approx 60\%$, mainly due to the (25 mm) thick lead layer. The 225 mm of polyethylene improve the gamma reduction by $\approx 10\%$ and reduce cosmic neutrons by $\approx 20\%$. A thicker layer of lead would not improve the suppression of gamma ray background (inner contamination and radon intrusion), but will increase the neutron flux (see Fig. 5 and Fig. 6)

Data taking The TPC detector acquired in total 142 d of background data and 203 h of tracking data. The improvement in the exposure time allows the statistic errors to be reduced relative to 2003 data, resulting in a better upper limit for the axion to photon coupling constant compared to 2003.

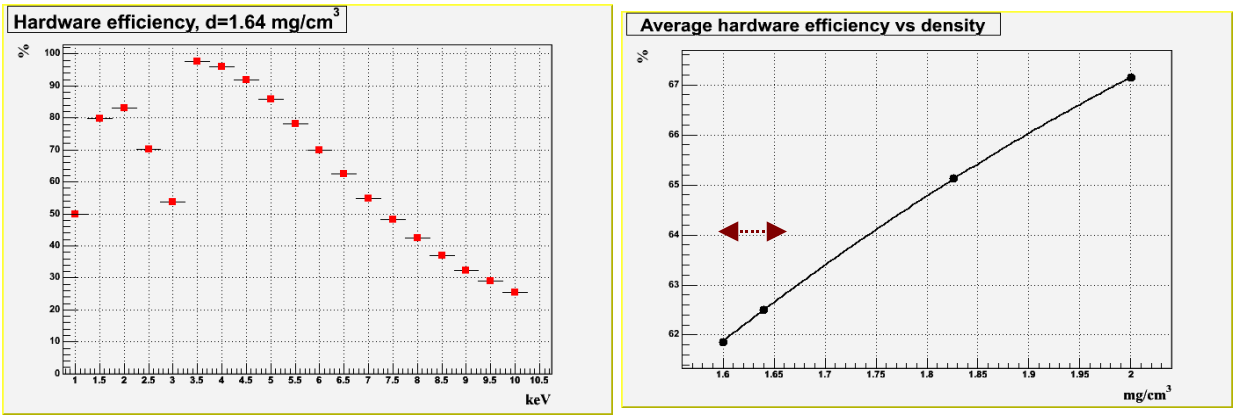

Figure 7: Left: Micromegas photon detection efficiency. Right: The average detector efficiency vs gas density. The region of interest for the 2004 experimental conditions is marked with the arrow.

5 Micromegas Detector

Detector Improvements The new Micromegas model was specially designed to eliminate the cross talk effects present at the V 3 detector model (the detector used in 2003) and to improve the quality of the strips. As a result, both goals were achieved with the new V 4 Micromegas (the substitute of the V 3 detector) detector ("dead" strips $< 1.3\%$) and valuable information from the spatial distribution of the charge produced after an event was used effectively in the analysis. Moreover, a faster VME digitizing board was installed (which records the time structure of the mesh pulses) reducing the detector's dead time (14 msec, less than 1.5% of the data rate) and an automated manipulator for the calibration source made the data acquisition user friendlier.

The smooth operation of the improved V 4 Micromegas detector during the 2004 data taking period, combined with the development of more effective off-line analysis techniques, allowed for further reduction of the background level (≈ 2.5 times less than 2003) while maintaining a higher overall efficiency of the detector compared to the V 3 model.

Background Simulation In order to investigate the properties of the V 4 model and to understand the origin of the background, the GEANT4 package was used for a Monte Carlo simulations. The V 4 detection efficiency of photons entering transversely (not taking into account the geometrical reduction of the efficiency due to the strong-back supporting the window of the detector) is shown in the left image of Fig. 7 and the effect of the gas density variation (due to pressure and temperature variation) on the average detector efficiency is shown in the right part of Fig. 7. Moreover, it has been found that the detector's background is induced by muons hitting the surrounding materials, gammas from airborne ^{222}Rn, neutrons, and X-rays present around the detector.

Data analysis Due to the stability of the detector and the experiment in general, it was possible to accumulate 196 h of high quality tracking data and 1500 h of background data (77 h and 810 h respectively in 2003). The software analysis was improved by using a Fisher discriminant method which combines information from the time characteristics of the mesh pulses (thanks to the MATACQ Board) and the charge distribution over the strips. The system's stability can be demonstrated through time structure of the pulses (0.5% variation!) and the moderate gain variation ($\approx 10\%$ on a week scale) which was corrected by daily calibration measurements. The resulting background

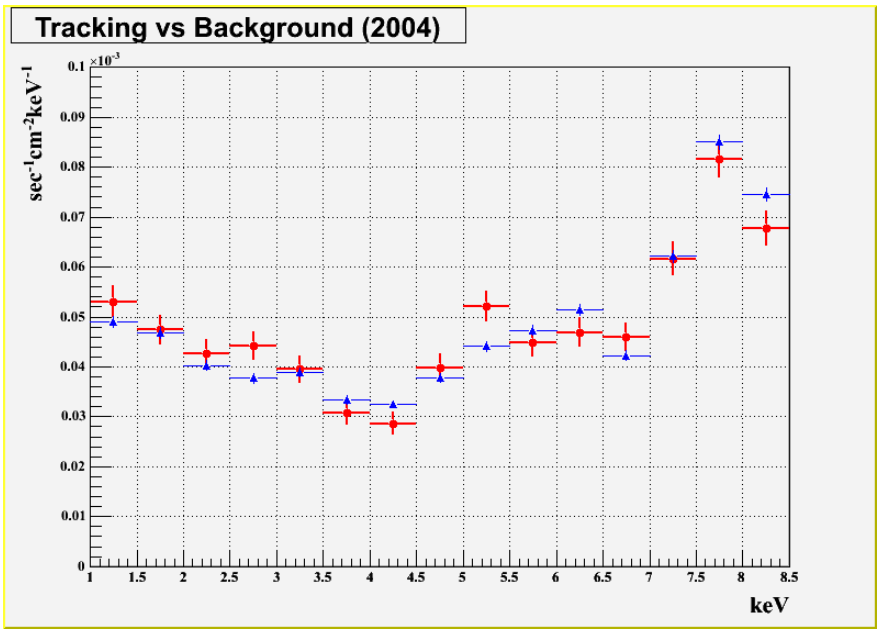

Figure 8: Comparison between the spectrum accumulated with the Micromegas detector during axion sensitive conditions (red) – tracking spectrum – and the background spectrum (black).

level of the Micromegas detector is 4.82×10^{-5} counts cm^{-2}sec^{-1}keV^{-1} in the 1–8.5 keV region (see Fig. 8) with 92% uniform software efficiency.

6 The X-ray Telescope and pn-CCD

The pn-CCD detector has shown a stable performance over the time of the 2003 data taking phase. A change in the pn-CCD detector hardware configuration was not necessary and is not foreseen for the second phase of CAST. The background level of 7.96×10^{-5} photons cm^{-2}sec^{-1}keV^{-1} is comparable to the background we measured shortly after adding the new internal and external lead shielding components in 2003. This differential photon flux translates in a count rate of ≈ 0.1counts/h. Taking the short observation times of 1.5 h per mass step during Phase II of CAST into account, the pn-CCD detector will quasi be free of background .

6.1 Telescope Operation 2004

To verify the pointing stability of the X-ray telescope system, we used an X-ray source that is installed on the TPC end of the magnet and illuminates the aperture of the X-ray telescope. The observed X-ray signal has a spot-like spatial distribution. The position of this spot on the pn-CCD detector can be used as a reference to monitor the stability of the alignment of the X-ray telescope relative to the magnet and to monitor the location of a potential signal. Measurements with this system were repeated regularly during the 2004 data taking period. Fig. 9 shows the observed spot position depending on magnet orientation before and after the 2004 data taking period. These measurements demonstrate that for the case of a positive signal, the location of the axion image of the sun would have been stable within one pixel diameter of the pn-CCD ($\approx 20''$). The stability of the position of the signal spot allows us to reduce the size of the region where we expect a potential

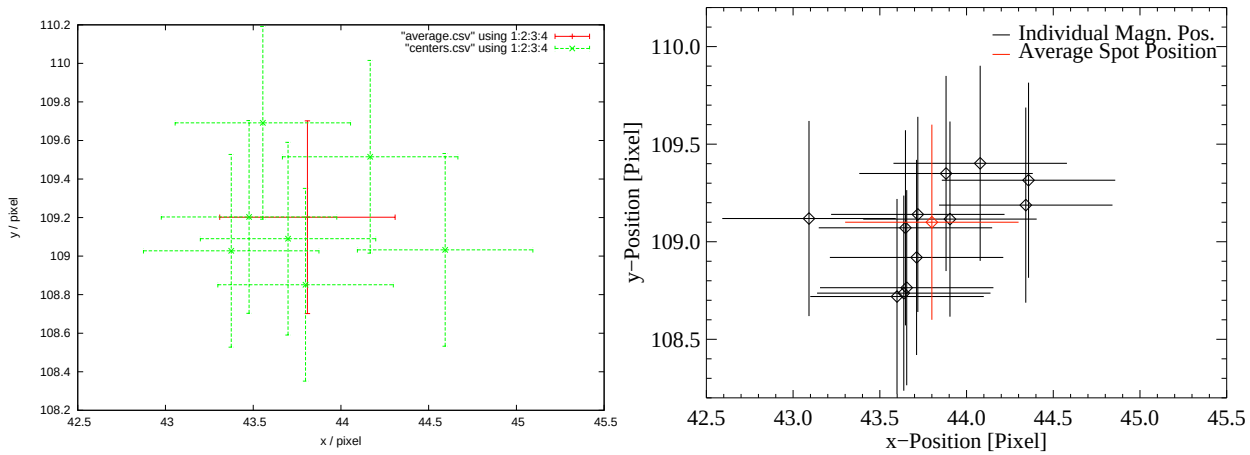

Figure 9: Left: X-ray spot position as observed with the pn-CCD depending on the magnet orientation before the 2004 data taking run. Right: The same measurement at the end of the 2004 data taking period.

axion signal on the pn-CCD chip below the dimensions predicted by the solar axion model and thus we can exploit the full potential of the X-ray optics.

6.2 Data Analysis

The preliminary analysis of the 2004 data yields 180 h of useful data during axion sensitive condition and 1723 h of background data (compared to 121 h of tracking data and 1233 h of background data in 2003). The preliminary results of the 2004 data demonstrate that we are able to improve the upper limit on the axion to photon coupling constant $g_{a\gamma}$ well below $g_{a\gamma} < 1.00 \times 10^{-10}\,\mathrm{GeV}^{-1}$ and can establish a limit that is better than the best limits known from astrophysical considerations. For this purpose, the software for the analysis of the pn-CCD data is further improved, incorporating the solar axion model (e.g. the shape of the axion spot).

In addition we made extensive systematic studies of the observed background depending on different operating conditions and different background subtraction methods, including toy Monte Carlo models to verify the derived upper limit and to characterize the influence of systematic effects. In collaboration with the University of Zaragoza, we started simulations with the GEANT4 package to characterize the observed background of the pn-CCD in more detail. One of the main intentions of the simulations is to estimate the influence of natural radioactivity on the overall background of the pn-CCD of CAST.

7 Sun Filming

Twice during a year, in spring and fall, we have the opportunity to verify the the pointing accuracy of the tracking system by direct optical observation of the sun (solar filming). These observation were repeated regularly during the past and the results of the measurements have already demonstrated that the pointing accuracy of the CAST system during the 2003 and 2004 data taking phase was better than the requirements. In the last years, the solar filming was done with a setup consisting of a webcam in combination with a small optical telescope. For the observations in spring 2005 we improved the system using an ST7 CCD camera and a better optics with 200 mm focal length.

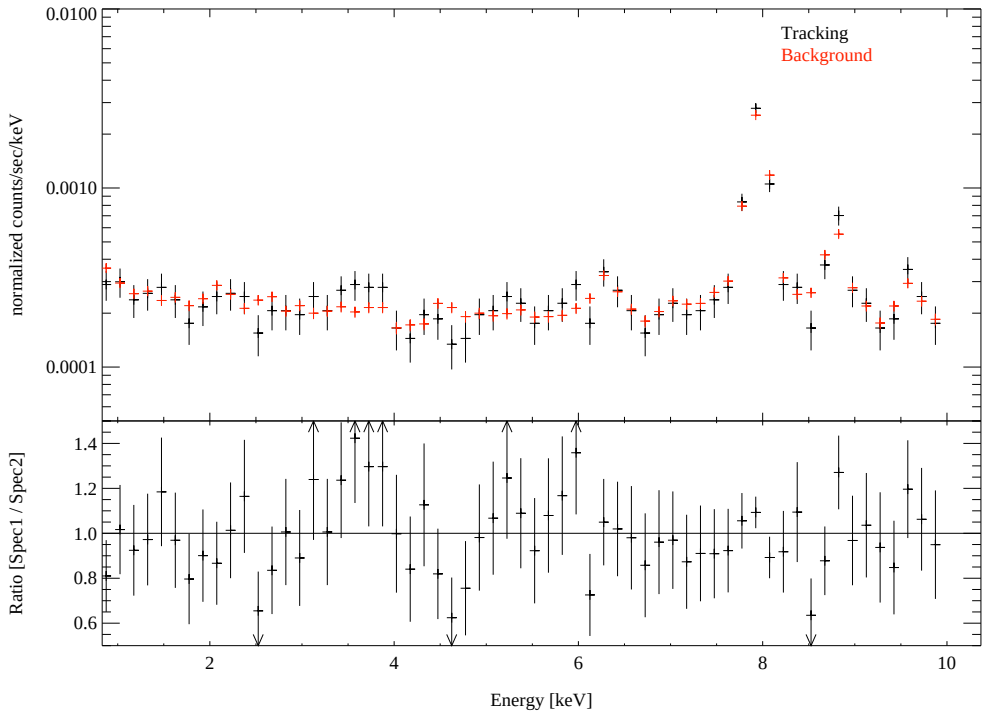

Figure 10: Comparison between the spectrum accumulated with the pn-CCD detector during axion sensitive conditions (black) – tracking spectrum – and the background spectrum (red).

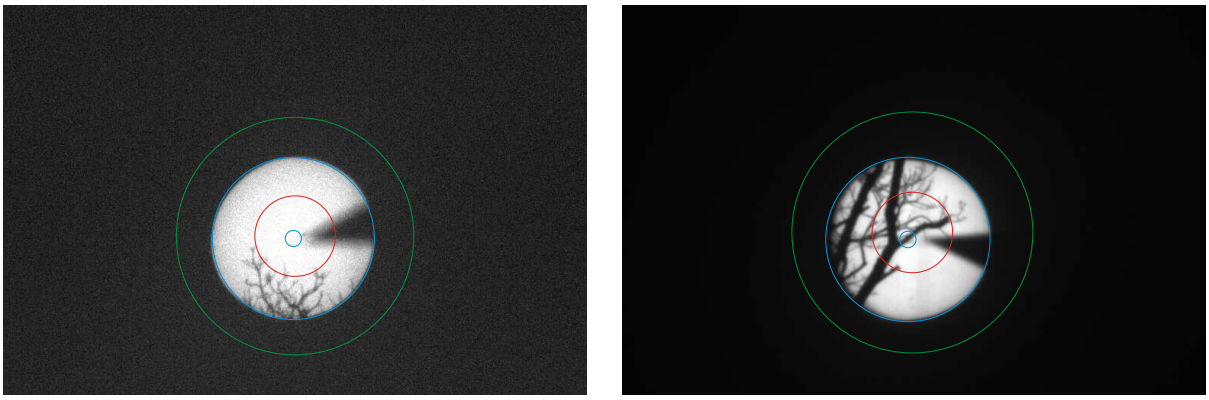

Figure 11: Left: Picture taken on March 16 with the optics of the CCD camera being focused at a distance of $30\,\mathrm{m}$. The green circle marks the center of the Taylor-Hobson-Sphere equipped with cross-wires that were used to align the optics, the red circle marks the acceptance region of the magnet bore, the large blue circle marks the disk of the sun, and the small blue circle the axion emission region ($\approx 10\%$ of $R_\odot$). Right: A similar picture taken on March 21 using a different focus setting and pointer.

In addition the concept to align the camera and the optics to the optical axis of the magnet was changed. This new setup improves the accuracy of the measurements and the imaging qualities.

To test this new setup we observed the sun in March 2005. Since the magnet configuration was changed compared to the usual operating conditions during the 2003 and 2004 data taking phase of CAST (e.g. shielding of TPC was removed) these observations can "only" be considered as test of the new CCD camera and optical setup for measurements during future data taking runs of Phase II of CAST. We observed the sun at three days, March 16, 17, and 21. On March 16 and March 21 the sun was observed in the so called filming mode, i.e. atmospheric effects are corrected by the tracking software and we follow the apparent position of the sun. On March 17 the same observation was repeated without refraction corrections, which allows to determine the deviation between the apparent position of the sun and the calculated position where the sun is expected to be, i.e. the refraction correction code. In addition we tested different pointers that are used to align the optical camera system to the optical axis of the magnet.

The left image of Fig. 11 shows a picture taken on March 16 with the optics being focused to $30\,\mathrm{m}$, while the right image of Fig. 11 was taken on March 21, focused to $15\,\mathrm{m}$ using a more accurate pointer (triangular shadow). The center of the green circle marks the crossing point of the wires in the Taylor-Hobson-Sphere used to align the optics. The size of the disk of the sun and the axion "emitting" core (about 10% of the solar diameter) are indicated as a blue circle while the red circle shows the acceptance area of one magnet bore (about 16'). In summary we can conclude that the new system is operating well and allows to verify the tracking precision with a significantly better accuracy compared to the past (required precision $\leq 1'$).

8 Second Phase of CAST

During the years 2003 and 2004 the CAST experiment was operated keeping the magnet pipes evacuated and therefore it was sensitive to the axion mass range up to $m_{\mathrm{a}} = 0.02\,\mathrm{eV}$ due to coherence effects. The second phase of CAST, where the magnet pipes will be filled with a suitable buffer gas can extend the sensitivity of CAST to higher axion rest masses $m_{\mathrm{a}} \lesssim 0.8\,\mathrm{eV}$.

8.1 Simulations

In order to operate the system safely at a temperature of $1.8\,\mathrm{K}$ with the magnet bore being filled with a buffer gas (avoiding condensation), $^4\mathrm{He}$ can safely be used up to a maximum pressure of $\approx 6\,\mathrm{mbar}$. For $^3\mathrm{He}$ the saturation pressure limit is $\approx 60\,\mathrm{mbar}$. In order to be sensitive to different axion masses, the gas pressure has to be systematically changed. According to our simulation results, the optimum number of individual mass steps or pressure settings for the $^4\mathrm{He}$ phase is 74 settings (steps of $\Delta P = 0.08\,\mathrm{mbar}$). For the $^3\mathrm{He}$ phase more steps are necessary to accurately scan the mass region and to avoid insensitive gaps due to a too rough sampling of different axion masses. Our results yield an optimum number of 590 individual pressure settings for the $^3\mathrm{He}$ phase (steps of 0.08–$0.1\,\mathrm{mbar}$). In this way, all axion rest masses, up to $\approx 0.8\,\mathrm{eV}$, will be equally covered (two consecutive peaks overlap at least at 50% of a peak height, see Fig. 12). Due to the limited observation time, several pressure settings may have to be measured per day.

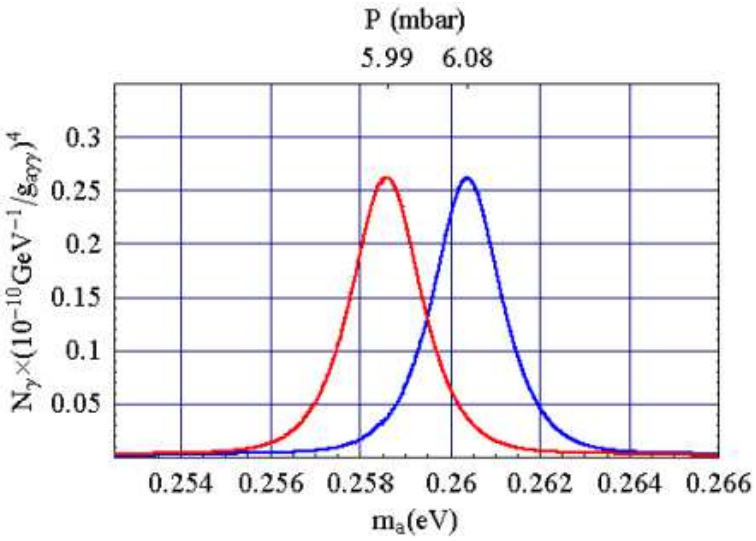

Figure 12: Number of expected photons depending on axion mass for two specific pressure settings. The two curves should have significant overlap to avoid insensitive gaps in the axion mass sampling during Phase II of CAST.

8.2 ^{3}He gas system

Specifications Taking all boundary conditions for CAST Phase II into account (physical and technological), we can summarize the following requirements for the ^{3}He gas system:

- It must provide gas in the magnet bore at a density that is stable to 10^{-4} over the time of an observation ($\approx 2\,$h).
- It must be able to recover the ^{3}He gas from the magnet bore for the case of a magnet quench such that the cryogenic windows will not break.
- It must provide safe storage and handling of the ^{3}He gas such that ^{3}He gas losses will be minimal ($< 10^{-3}$ during 2 years of operation).
- It must provide a storage volume for the gas ($\approx 0.5\,\mathrm{m}^3$).
- The required pumping speed for the inlet pressure is $\approx 500\,\mathrm{m}^3/\mathrm{h}$ from $0.1\,$mbar to $500\,$mbar.
- It must be based on a gas dynamic design minimizing dynamic pressure losses.

These specifications are subject to changes after the quench tests with ^{4}He in the bore tubes have been finished and analyzed.

Gas recovery during quench A schematic view on the design of the Helium gas system is shown in Fig. 13. The existing vacuum components and electromagnetic valves at the gas exits from the magnet bores will be used for a recovery system for the ^{3}He gas. The present temporary vacuum pumps used for the evacuation of ^{4}He will be replaced by the recovery system for ^{3}He. The electromagnetic valves will deliver the gas into conical tapers and metal bellows compensators leading to a gas dump with a volume of $0.5\,\mathrm{m}^3$, which is a $250\,$mm pipe mounted on top of the magnet (item 5). This item includes its mechanical supports and a $100\,$mm line with flexible

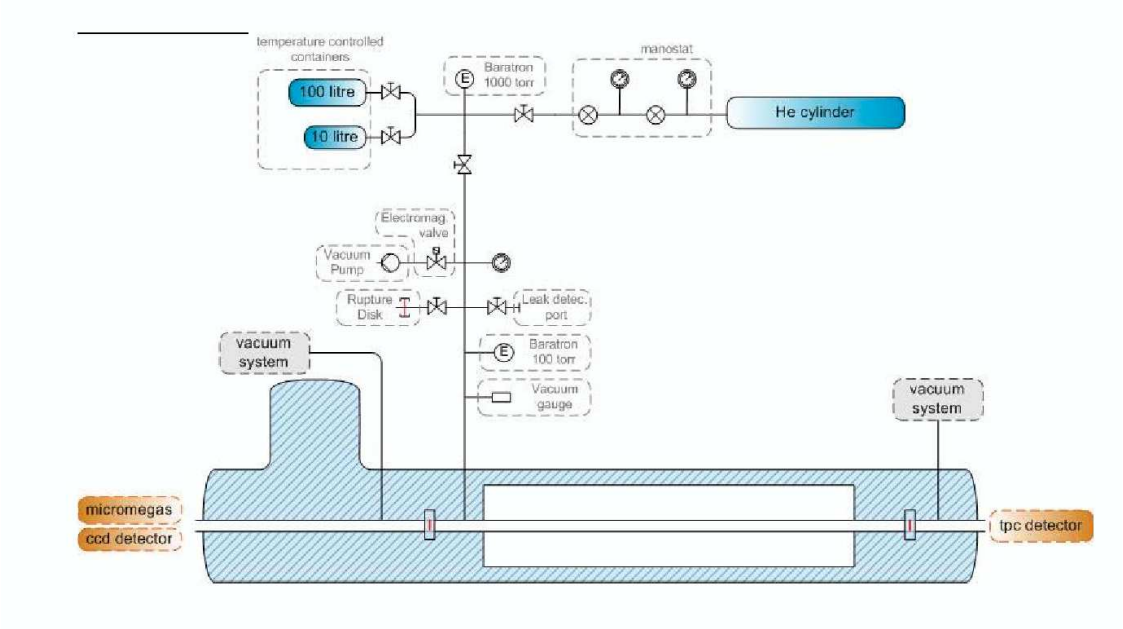

Figure 13: A schematic overview on the design of the CAST Phase II Helium gas system.

sections leading to the $^3\mathrm{He}$ pumps. The pumps must be able to recover about $500\,\mathrm{l}$ STP of gas in about $30\,\mathrm{sec}$, at an average pressure of a few hundred mbar. This specification follows from the dynamic pressure at the cold windows, which must not break, and from the dynamic and frictional pressure drop in the narrow pipes linking the bore tubes from $1.8\,\mathrm{K}$ to room temperature. The safe pump speed requirement is then about $500\,\mathrm{m}^3/\mathrm{h}$. All pumps in the cascade will have to be able to withstand the peak gas load, which is reduced by the smoothing effect of the gas dump volume. The pumps can stand on the floor near the magnet girder, if the $100\,\mathrm{mm}$ line leading to them from the dump will have suitable flexible sections.

Stable gas density The gas density in the magnet bores is stabilized to better than 10^{-4} by running at a constant amount of gas in the closed volume, where the amount of gas outside the magnets bores is minimized. This will enable to run at a rather constant gas density, despite of the small variations of the temperature of the magnet.

Reproduction of previous density setting The monitoring of the gas density is done by measuring its pressure and temperature. Both parameters are obtained by using the MKS Baratron pressure gauges, and by a resistance thermometer, which have sufficient relative accuracy for reproducing the pressures settings to better than $0.01\,\mathrm{mbar}$ or 10^{-4} times the pressure.

The absolute accuracy of the density The absolute density can be measured only to about 2×10^{-3}. The limiting parameter is the accuracy of the sensors and instruments used presently for the thermometry.

8.3 Cold Windows

By the end of 2004, it became clear that the ultra-thin windows (based on coated polyimide foils $< 1\,\mu\mathrm{m}$) being developed by METOREX(FI) were not sufficiently robust for use in CAST. Two al-

ternatives were considered instead, Beryllium windows ($25\,\mu$m thickness) purchased from external expert companies (e.g. METOREX and BRUSH-WELLMAN) or windows using polymer films based on existing expertise developed within CAST for gaseous detector windows facing vacuum.

Beryllium is technically the most attractive solution in terms of X-ray transmission versus vacuum tightness. But a potential problem with the use of Beryllium is the consequences of a comprehensive breakage of a window causing contamination of the cold bore, piping and pumps. This could imply very high costs and long delays resulting from the obligatory use of expert companies to make contamination tests and then execute the clean-up of the system. Contaminated pumps would also have to be replaced.

As a result, for the 2005 test run, it was decided to concentrate the efforts on a conservative and robust window developed by the CEA/DAPNIA inside the CAST collaboration. The requirements for such a window are the following:

- The windows have to be mechanically strong and robust in view of the first operation of CAST with helium gas in the cold bore.
- The required leak tightness at $1.9\,$K should be about 2 orders of magnitude below the required leak tightness of $10^{-6}\,\mathrm{mbar\,l\,sec^{-1}}$.
- The windows should be transparent in the visible to allow laser alignment checks of the focusing optics via the cold bore.

An extensive program of tests has been defined to investigate different window materials like Polypropylene (PP), Parylene N, Mylar, and Polyimide. Different samples of these materials will be helium leak tested in the CERN AT-Cryolab at pressure differences up to $1\,$bar and at temperatures down to $1.9\,$K. A cold window which was forseen for tests is shown in Fig. 14. It consists of a custom 316LN vacuum flange designed to be coupled on one side to the CF63 vacuum flange at the exit of the cold bore and on the other side to the vacuum lines extending from the cold bore to the detectors. The center of the flange is electro-eroded to form a $5\,$mm deep "strong-back" consisting of $5.2\,$mm square cells separated by $0.3\,$mm thick walls. The average geometrical transmission of this structure is 89%.

The polymer foil building the window, is glued onto the strong-back of the flange (cold bore-side) with a minimal glue layer (thickness $<<\,50\,\mu$m). The glue is applied to both parts, the perimeter ring and the struts of the strong-back. In the soft X-ray range 0–$8\,$keV, the polymer with the best transmission per unit thickness is Polypropylene (PP). In view of the limited time available for R&D of the windows, the thermal vacuum tests have been concentrated on PP as foil material. A summary of the results of the thermal and leak test is given in Table 2.

The $4\,\mu$m PP foil was found to have a high leak rate and also wrinkled after being subjected to the thermal and mechanical stresses. The $12\,\mu$m PP was much improved at room temperature (RT) and the leak rate actually decreased when lowering the temperature. However, the leak rate rose again at the lowest temperatures due to pin-holes. The $23\,\mu$m PP windows have proven to be very reliable; a leak rate $\ll 10^{-8}\,\mathrm{mbar\,l\,sec^{-1}}$ at $1.9\,$K has been measured on each of the 5 windows tested. Fig. 15 shows the typical behavior of the windows during a leak test. At room temperature, a leak rate of about $1\times10^{-5}\,\mathrm{mbar\,l\,s^{-1}}$ is observed which is dominated by helium permeation through the foil. The permeation signal decreases rapidly as temperature is decreased towards $1.9\,$K. In the absence of pin-holes in the foil, the leak rate measured at low temperatures is well below $1\times10^{-8}\,\mathrm{mbar\,l\,sec^{-1}}$ and is dependent on the helium background in the Cryolab.

One problem did arise with the PP foil, namely that it is difficult to achieve a good adherence of standard glues (e.g. Araldite 2011) to the foil. Under the guidance of L Hominal TS-MME,

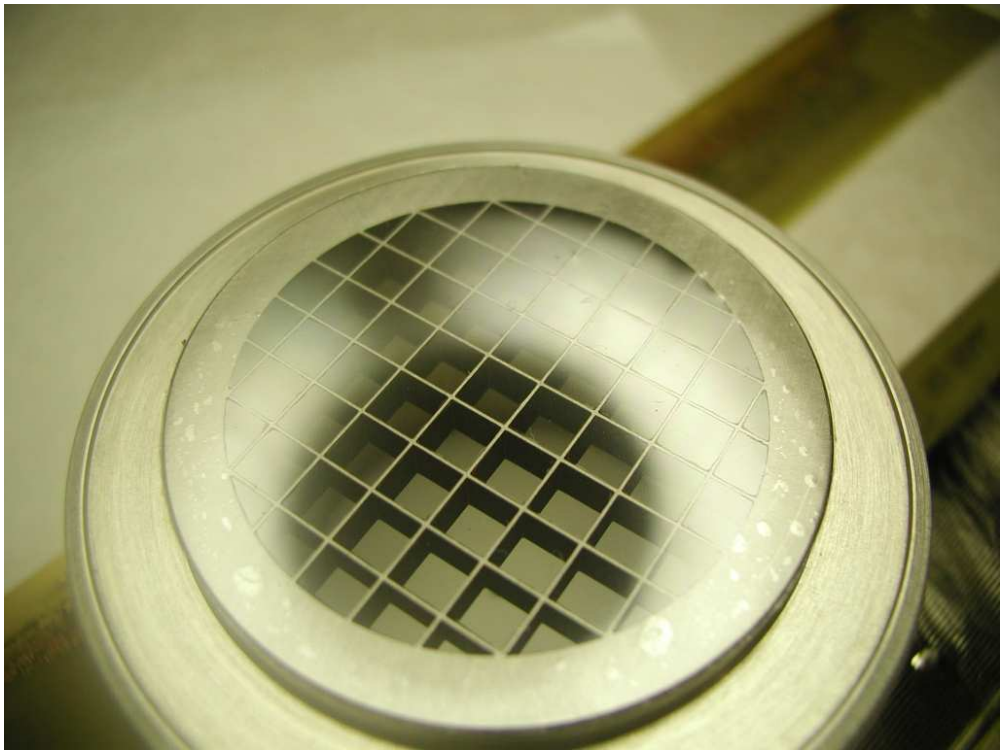

Figure 14: A sample cold window before the cryo and vacuum tests. The flange and the cell structure of the strong-back is visible. The window itself is glued from the back side to the strong-back.

several polyurethane glues were found to have good adherence and Araldite 2018 has been chosen for the CAST windows for 2005. Two leak tests have been successfully performed on window flanges constructed with this glue. A program of peeling tests is underway (TS-MME) to test compatibility of glues with various foils for future window development. In order to increase the safety of the 2005 windows, a thin steel top cover will be glued on top of the glued foil around the perimeter to prevent any risk of the window foil starting to peel. Fig. 16 shows a comparison of the theoretical transmission curves (the transmission of the strong-back is not included) for $12\,\mu$m PP, $23\,\mu$m PP, $25\,\mu$m Be together with two curves demonstrating the amount of absorption by the helium buffer gas at 1.8 K at pressure of 6 and 60 mbar.

The 2005 windows are optimized for robustness and reliability and hence the transmission is not yet fully optimized. The transmission of $23\,\mu$m PP is slightly worse than a $25\,\mu$m Be window, the fraction of the axion X-ray spectrum ($0 - 8$ keV) transmitted by the strong-back (89%) and window foil combined is estimated at 75% ($25\,\mu$m Be) and 71% ($23\,\mu$m PP). However, it can be seen from Fig. 16 that at Helium pressures above 6 mbar, the low energy cut-off due to absorption by the helium gas itself dominates over the absorption in the window material. In summary, the CAST window for 2005 will be $23\,\mu$m PP on a 5.2 mm square cell strong-back 5 mm deep using Araldite 2018 glue. A top cover will be glued over the perimeter of the window as an additional protection. Eight windows will be made, four for installation and 4 spare windows.

The status of the windows is as follows: the 316 LN window flanges are machined (Univ. Freiburg), and today the strong-backs on 5 out of 8 flanges have been electro-eroded with the remaining strong-backs to be completed by week 26. The tooling for the production gluing has been assembled and tested at SACLAY. The gluing will start during week 27 at a rate of 2 windows

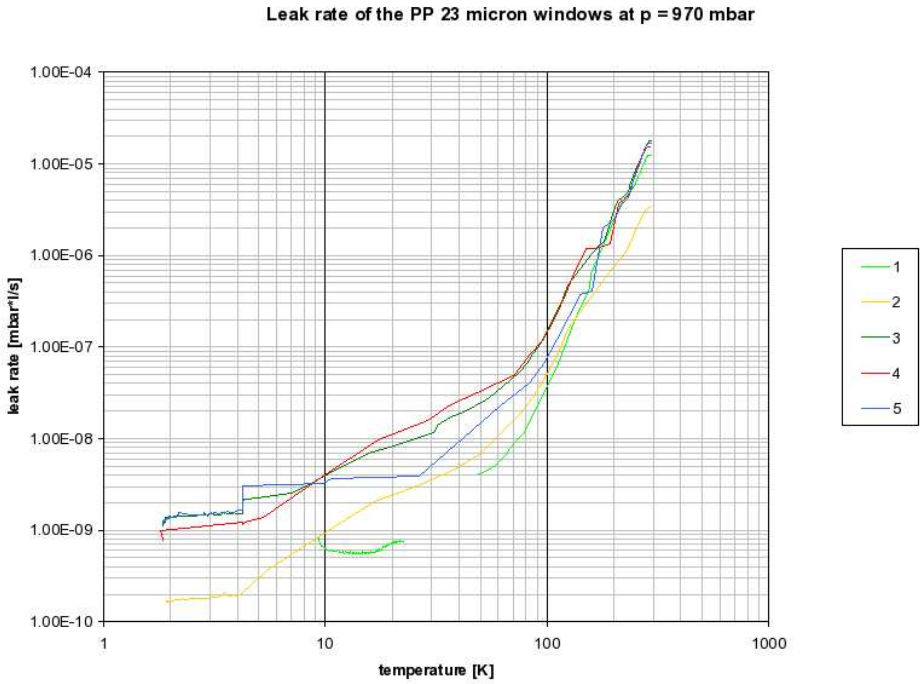

Figure 15: Helium leak rate depending on temperature for 5 different test windows with a foil thickness of 23 μm.

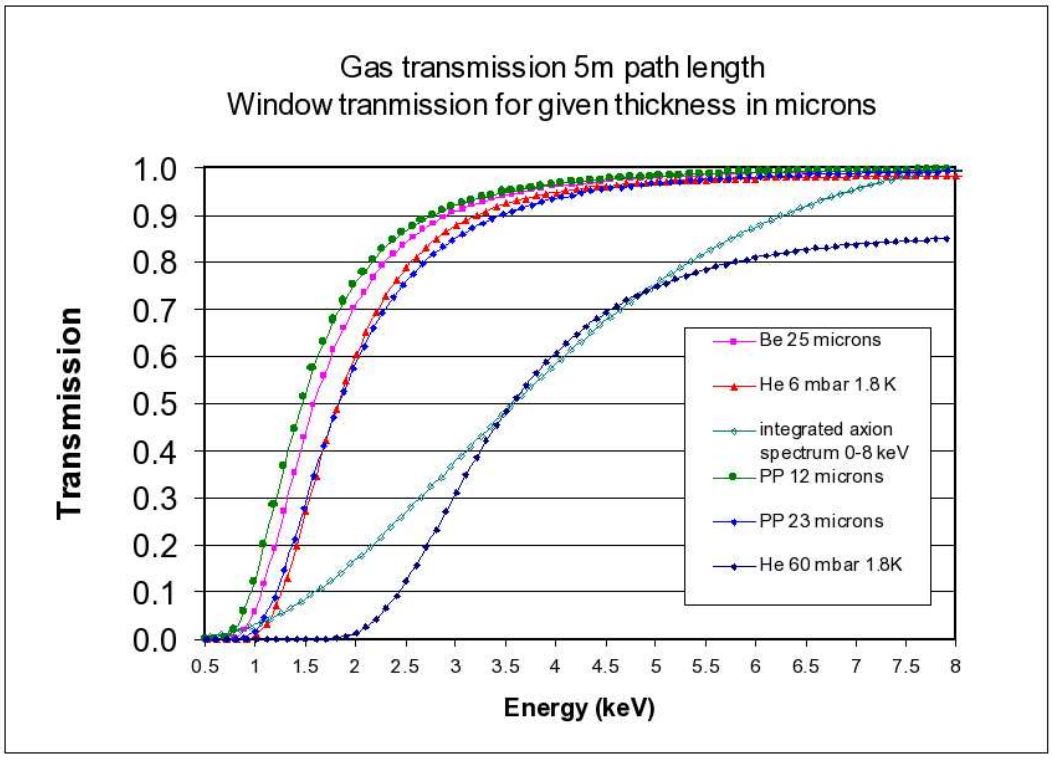

Figure 16: Theoretically calculated window transmission for different foil materials. The calculation includes absorption by the buffer gas for different gas pressures.

Table 2: Summary of PP helium leak tests with 1 bar Helium pressure difference.

Polymer	Thick. [μm]	Glue type	Test flange	He leak rate [mbar l sec^{-1}] at RT	at 4.2 K	at 1.9 K	at RT	Comments
PP	4	A 2011	S1	7×10^{-2}	10^{-1}	9×10^{-2}		Foil wrinkles
PP	12	A 2011	S2	5.5×10^{-5}	1×10^{-5}			Foil - no wrinkles
PP	23	A 2011	S2	1×10^{-5}	1×10^{-9}	2×10^{-9}		
PP	15	A 2011	S1					Poor adherence found before test
PP	23	A 2011	S2	3×10^{-6}	3×10^{-10}	2×10^{-10}	5×10^{-6}	Poor adherence after test
PP	23	A 2011	F1	2×10^{-5}	2×10^{-9}	1×10^{-9}	2×10^{-5}	Top cover (no glue on strong-back struts). 2 cold cycles
				2×10^{-5}	8×10^{-10}	6×10^{-10}	1×10^{-5}	
PP	23	A 2018	S2	1×10^{-5}	1×10^{-9}	8×10^{-10}	2×10^{-5}	
PP	23	A 2018	F2	2×10^{-5}	2×10^{-9}	1×10^{-9}	1×10^{-5}	Glued only on perimeter

per week. The windows will be then be tested in the AT-Cryolab at a rate of 2 per week such that the first four windows can be installed in week 33.

The 6 month R&D available before Spring 2006 allows us to aim at producing an optimized and thoroughly tested window designed to comfortably withstand any quench conditions inside CAST. The strong-back will be optimized to decrease the geometric absorption losses using both calculations and pressure tests on prototypes. The present testing program for polymer foils and coated polymer foils will be completed with the aim of optimizing the X-ray transmission through the foil. The final choice will be thoroughly tested.

8.4 Micromegas and Phase II

The Micromegas line will be upgraded for Phase II from 2006 onwards in order to accommodate for the new focusing optics. Profiting from the fact that the converted photons will be focused in a spot of less than 2 mm diameter, the active area of the detector can be reduced by a factor of two. This allows to insert additional shielding. Furthermore the Micromegas detector will be upgraded to improve its efficiency.

Shielding The shielding will protect the Micromegas detector from a fraction of the cosmic rays and natural radioactivity. The TPC experience shows that the reduction of the mean background level can be of the order of a factor of 4. The shielding will consist on 0.5 cm of copper and 2.5 cm of lead and a Radon shield provided by a permanent flow of N_2. The gas tightness of the detector will be obtained by a plexiglass enclosure. On the plexiglass, blocs of polyethylene of 20 cm thickness will cover the whole detector. The shielding will have a 4π coverage and will be composed of a cylindrical central part and a circular end cap that will close the cylinder. The central part will be on rails to ease the insertion of the detector. Background studies at the University of Zaragoza are in progress, that will estimate the effect of the shielding taking into account the material of the detector and its environment. The shielding will be designed and build at the University of Zaragoza once the plans are finalized.

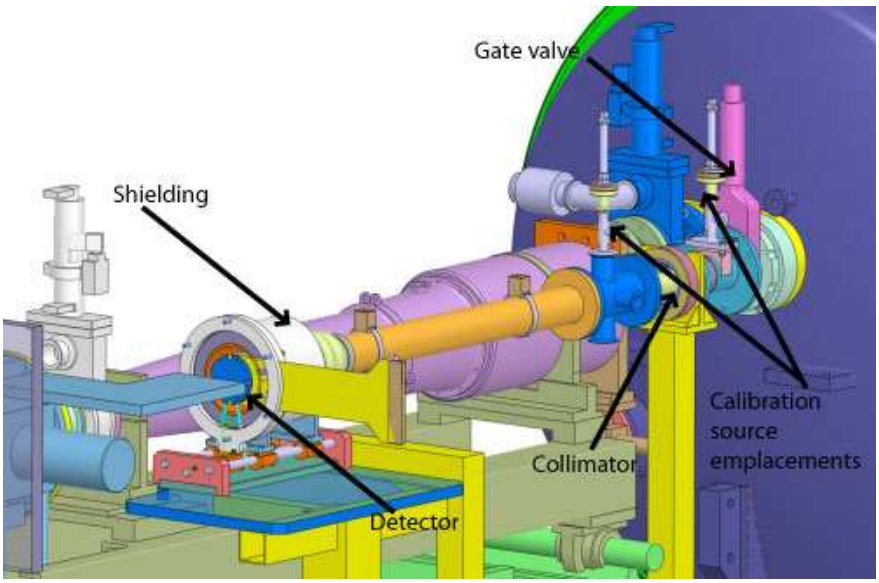

Figure 17: Sketch of the Micromegas detector and the new X-ray telescope being installed at the CAST magnet.

The Micromegas detector in operation during Phase I had an active zone of $50\,\mathrm{cm}^2$. The active zone of the upgraded detector will be reduced by a factor 2, consequently decreasing the number of electronic channels and more important giving extra space to accommodate for the new shielding. The Argon/Isobutane mixture used during Phase I allowed for a conversion photon efficiency of 80% in the relevant interval of energy for solar axions. We are studying the possibility to use a mixture of Xenon that would allow for a 15% improvement of the gas conversion efficiency. The decision will be made in terms of efficiency, gain, and stability of the detector and if possible non-flammability of the gas. As Xenon is an expensive gas ($\approx 15\,\mathrm{EUR/L}$) a more sophisticated gas system will be designed for the operation of the detector in a semi-sealed mode by using a calibrated leak that will maintain the gas conditions constant. Fig. 17 shows an overview of the new Micromegas setup including the collimator optics. The system has been carefully designed to allow an in situ alignment of the collimator as well as a monitoring of the system during data taking.

9 Second X-ray Optics

An X-ray optics can increase the sensitivity of CAST to the axion coupling constant by reducing the potential signal area on the detector from the width of the magnet bore to a few mm, leading to a significant reduction in the background. Currently, the CAST experiment employs the prototype ABRIXAS telescope on one of the four magnet bores. In July 2004, we considered the feasibility of constructing and installing a second X-ray optic to work in conjunction with the Micromegas detector. A detailed multi-parameter study led to a collimator design that should achieve 35% total throughput in a $1.6\,\mathrm{mm}$ wide spot. This performance is nearly identical to the current X-ray telescope.

Design Study Grazing incidence reflective X-ray optics can readily provide the large collecting area in the soft X-ray band ($0.5 < E < 10\,\mathrm{keV}$) needed for CAST. Either a telescope or collimator

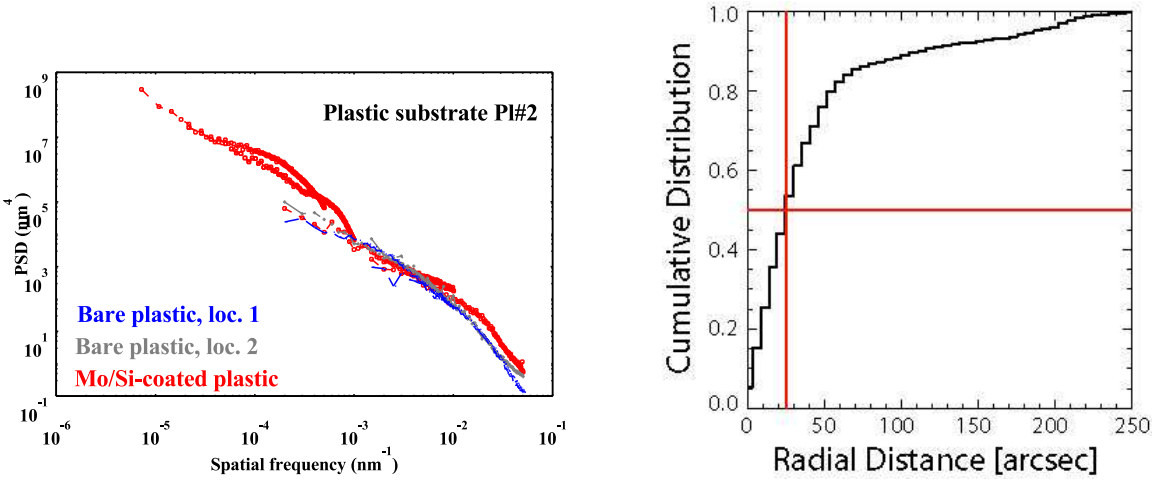

Figure 18: Left: Power spectral density (PSD) measurement of a prototype optic obtained with from Zygo and AFM measurements. The micro-roughness is $\sigma < 3.0\,\mathrm{A}$. Right: $8\,\mathrm{keV}$ measurement of the encircled energy function of a prototype optic. The half-power diameter (HPD) is $50''$.

is an appropriate design to focus the wide, uniform solar region observed by CAST. For the same graze angle, a telescope has a focal length half that of a collimator.

On the other hand, a telescope requires two reflections to image, while a collimator requires only one. At these energies the reflectivity R is less than unity, such that the telescope throughput is proportional to R^2, while that for a collimator is proportional to R^1. After incorporating these factors with other considerations, like the limited space in the experimental hall and the cost and complexity to construct the optic, we determined the optimal design for CAST is a collimator with the properties summarized in Table 3.

Polycarbonate Optics Traditionally, reflective X-ray optics have been made from monolithic glass substrates ground and polished to the appropriate shape or via replication from a precision metal mandrel. More recently, a collaboration that includes LLNL has fabricated optics from segments of thermally formed glass. LLNL has continued to explore novel fabrication techniques and recently has developed a proprietary process for making substrates from polycarbonate. The key parameters for a reflective X-ray optical substrate are excellent micro-roughness ($\sigma \leq 5\,\mathrm{A}$) to ensure high reflectivity and low scattering and excellent figure (low spatial-frequency) errors to ensure proper focusing capabilites. Optical and X-ray metrology on prototype substrates indicate excellent performance, as shown in Fig. 18. Prototype optics coated with iridium will be tested at the end June.

Schedule After evaluating the prototypes, the fabrication process will be refined and the final substrates will be produce in the summer 2005. After coating with iridium, the nested shells will

Table 3: Basic Properties of CAST X-ray Collimator

Nested Shells	Length	Focal Length	Coating	Throughput	Focus Spot-Size
14	125 mm	1.3 m	Iridium: 350 A	36%	1.6 mm

be assembled into the final collimator configuration by October this year. Calibration of the optic will be performed at PANTER test facility with our collaborators from MPE. Concurrent to the construction of the collimator, we are developing a detailed alignment plan for the installation of the optic at CAST. Regular meetings between the groups at Saclay and LLNL, in frequent consultation with the larger collaboration will guarantee a smooth integration into the experiment with minimal disruption to on-going operations.

10 CAST Schedule

The original schedule for CAST in 2005 was to develop X-ray cold windows in the first half of 2005 and then install them around the middle of 2005. In parallel a provisional $^4\mathrm{He}$ gas system was to be designed and built. This would allow quench tests with X-ray cold windows installed together with low pressure $^4\mathrm{He}$ fillings in the cold bore. By measuring the pressure of the $^4\mathrm{He}$ gas, the temperature response of the gas filling during a quench could be calculated. The temperature rise, plus the rate of change of temperature are crucial to the design of the final $^3\mathrm{He}$ gas system to be used in 2006 and 2007. Provided the tests were successful, test runs and even some low-pressure $^4\mathrm{He}$ data taking were envisaged for the end of 2005.

At the end of 2004, another option was studied, which had significant advantages. Namely, to open the magnet cryostat in spring 2005. This allowed an early opportunity to inspect the interior of the cryostat. As a result, instrumentation for the Helium system could already be installed (temperature probes and heating circuits to regulate the temperature of "dead" volumes between the cold bore and the exterior of the cryostat). In addition, cold windows with a solid $5\,\mathrm{mm}$ steel disc (solid windows) were installed to separate the cold bore from the vacuum lines to the detectors. This gave good experience for the future installation of the fragile X-ray cold windows and will permit the initial quench tests to be performed without any risk of breakage of the fragile windows. Finally this allowed more time to develop the X-ray cold windows in parallel.

The early start has also accelerated the ordering of key components (for use in $^4\mathrm{He}$ and $^3\mathrm{He}$ systems) and the fabrication of the provisional $^4\mathrm{He}$ gas system. In addition the fast monitoring system for the quench transients and the debugging of the temperature and pressure instrumentation has been advanced.

The early opening also permitted CAST to investigate the small helium leak inside the cryostat. Whilst the leak could not be isolated at room temperature, a suspect metal joint was replaced by a welded joint and the cryostat was instrumented with vacuum gauges and a large turbo pumping system was installed at each end of the magnet. After closing the cryostat, systematic volume leak tests of each helium circuit in turn revealed that the helium leak was still present and was localized to the MFB liquid $^4\mathrm{He}$ reservoir. Magnet behavior since the subsequent cool down has already shown that the spikes in the cold bore temperature experienced in 2004 have been attenuated to the point of insignificance by the enhanced pumping system.

At present all systems needed to perform the quench tests with solid cold windows are installed and the program of tests has started. The tests are expected to last for a further 2 weeks. The magnet will then be warmed up and there will be a period available to add extra instrumentation inside the cryostat. Mid-August is the milestone for the installation of the four X-ray cold windows (four reserve windows will also be made).

The magnet cool down will take place in early September and then the TPC plus shielding will be added. At the end of September, the GRID survey of the magnet will be made and also direct observations of the sun will be made as a crosscheck. In parallel, test $^4\mathrm{He}$ fillings of the magnet

cold bore will be made and the reproducibility and stability of the pressure settings will be tested (also with magnet at different vertical angles).

After the GRID, the magnet will be powered and the experiment prepared for $^4\mathrm{He}$ data taking in the 0–6 mbar pressure range. Our goal is to complete our tests then to take as much data as possible before the winter shutdown.

References

Bahcall J.N., Pinsonneault M.H., 2004, Phys. Rev. Lett. 92, 121301

Hannestad S., Mirizzi A., Raffelt G., 2005, ArXiv High Energy Physics - Phenomenology e-prints

van Bibber K., McIntyre P.M., Morris D.E., Raffelt G.G., 1989, Phys. Rev. D 39, 2089

Zioutas K., Andriamonje S., Arosov V., et al., 2005, Phys. Rev. Lett. 94, 121301